scientific reports

OPEN

Unequally-spaced slot strategy for radiation null reduction in single SIW-embedded antenna element

Meha Agrawal[1✉], Ravi Yadav[2], Slawomir Koziel[3,4] & Anna Pietrenko-Dabrowska[4]

The incorporation of higher-order modes (HOMs) can substantially augment the antenna gain and bandwidth, but this improvement is typically accompanied by compromised radiation performance including radiation nulls and higher side lobe levels. In this study, an inventive strategy is introduced to reduce the radiation nulls and the side lobe levels of a single antenna element by positioning multiple slots of the radiating element at unequal spacing. Dual hybrid HOMs are analyzed inside a substrate integrated waveguide-based cavity to design a wide band, enhanced gain dual-polarized antenna. The radiating element of the antenna is designed with multiple slots positioned at unequal spacing but symmetrical along the origin. This methodology provides three-fold advantages: a reduction of side lobes, an adjustment of phase center, and a significant reduction of radiation nulls. The antenna has been fabricated, and experimentally validated. The antenna exhibits a reduction in radiation null to − 0.5 dB, a phase adjustment of the main lobe to 0°, and a reduction in side lobe level from − 14.4 dB ($N = 2$, equal spacing) and − 15.5 dB ($N = 4$, equal spacing) a maximum of − 19.7 dB ($N = 4$, unequal spacing) at 12.35 GHz in the phi-0 plane. Excellent agreement between measured and simulated results corroborates the efficacy of the proposed approach. The significant improvement in the radiation performance of the single-element antenna design sets the antenna design apart from the state-of-the-art solutions.

Higher order modes (HOMs) in an antenna structure amplify the gain and bandwidth, this improvement carries a drawback: it introduces radiation instability[1]. The instability manifests itself through the emergence of radiation nulls in the broadside direction, particularly across high frequencies[2]. Numerous studies have utilized HOMs to enhance gain and bandwidth; however, a noteworthy gap exists in their attention to the radiation pattern, which reveals a null in its distribution. A null of − 25 dB is observed in the E-plane radiation pattern at ±60° [3]. Similarly, a radiation null of − 18 dB in the E-plane appears at ±35° [4], and a radiation null of − 30 dB and − 35 dB is observed at the two ports at ±27° [5]. Another antenna[6] utilizes HOMs and the radiation pattern becomes asymmetrical along with higher radiation nulls and higher side lobes. The level of radiation null of at least − 22 dB at + 60° is observed at all the frequencies. Dual HOMs are excited[7] to achieve a dual band response however, radiation null of − 35 dB at ± 35° is observed in E-plane radiation pattern. Therefore, it is essential to strike a balance between increased gain and stable radiation patterns. Achieving consistent and reliable performance across high frequencies and wide bandwidth poses a challenge in antenna engineering. Thus, the quest for enhanced gain and wide bandwidth highlights the necessity for adjustments in radiation performance to uphold dependable communication and sensing capabilities.

To address this gap, various techniques have been explored in the literature to reduce the radiation nulls and adjust side lobe levels. Among the commonly employed methods there are three prominent approaches: Tapered amplitude excitation[8–10], non-uniform excitation in uniformly spaced antenna arrays[11], and uniform excitation in unequally spaced antenna arrays[12]. The tapered amplitude excitation method is a relatively straightforward technique, involving adjustments solely in the amplitude distribution[9]. However, its applicability diminishes for larger arrays, and the achieved side lobe reduction is confined to a specific threshold[12]. Equally-spaced arrays with non-uniform excitation offer increased flexibility compared to the tapered amplitude excitation method. Nevertheless, this approach still encounters limitations in achieving precise side lobe reduction, and the associated feed design becomes increasingly complex. In contrast, unequally-spaced antenna arrays demonstrate

[1]Department of Electronics and Communication, Indian Institute of Information Technology Design and Manufacturing, Jabalpur 482005, India. [2]Faculty of Electrical and Computer Engineering, Technion Israel Institute of Technology, 3200003 Haifa, Israel. [3]Engineering Optimization and Modeling Center, Reykjavik University, 102 Reykjavík, Iceland. [4]Faculty of Electronics, Telecommunications and Informatics, Gdansk University of Technology, 80-233, Gdańsk, Poland. ✉email: anumeha19@gmail.com

a superior capability in terms of side lobe reduction. These arrays provide precise control over side lobe levels, which was challenging in equally spaced arrays. The specific side lobe level can be meticulously adjusted by varying the spacing between array elements[13]. However, the past research efforts for mitigating radiation nulls and side lobe levels have predominantly centered around antenna arrays and no method has been proposed for the improvement in radiation performance of a single antenna element.

This paper introduces the unequal spacing technique as a novel approach to reduce the radiation nulls and side lobes in a single antenna element featuring multiple slots. The foundational principle involves treating the radiating element, comprised of multiple slots, as an array with two or more slots strategically positioned at half-wavelength intervals or less. The initial focus involves a comprehensive study of hybrid HOMs within a SIW cavity, contributing to radiation nulls and higher side lobes. Further, based on the fundamental frequency of the SIW, unequal spacing between multiple slots is decided. Concurrently, the impact of unequally-spaced slots (USS) on radiation performance is studied through the examination of three distinct configurations—with two equally spaced slots (ESS), with four equally spaced slots, and with four unequally spaced slots. Building upon the foundation of dual hybrid HOMs, namely TE_{130}/TE_{310} and TE_{230}/TE_{320}, coupled with unequally spaced slots, a wideband, enhanced gain, dual-linearly polarized SIW-based antenna is designed, with improved radiation characteristics. The unequal spacing between the slots demonstrates a significant reduction in radiation nulls and side lobes and also facilitates electronic adjustment of the phase center of the main radiation lobe. An equivalent circuit model is constructed to investigate the influence of the antenna's design parameters. This model offers a detailed examination of the changes in various antenna dimensions correlated with equivalent variations in circuit elements. The final optimized design is fabricated and experimentally validated, showcasing a commendable agreement between simulated and measured antenna responses. Despite its improvement in radiation performance, the fabricated antenna also exhibits wide bandwidth and a high gain-to-size ratio (GSR). Consequently, this technique emerges as a promising means to exert precise control over the radiation performance of a single antenna element.

Methods
Dual hybrid higher order modes in SIW cavity
The modes inside a square shaped SIW structure are analyzed. The SIW cavity is designed by following the basic design rules[14,15]. The width and length of the SIW cavity is chosen to be 28.0 mm, the diameter of the vias is 1.0 mm, and the pitch is 2.0 mm. The shape of the SIW cavity is chosen to be square so that orthogonal degenerate modes (TE_{130}/TE_{310} and TE_{230}/TE_{320}) of the same frequency can be excited together. These degenerate modes are combined to form hybrid modes $TE_h(130, 310)$ also termed hybrid TE_{220} mode, and $TE_h(230, 320)$. The input impedance of the square SIW cavity is shown in Fig. 1. The real and imaginary curves of the existing modes are shown in the frequency range of 10.0 to 13.0 GHz.

First hybrid higher-order mode TE_{220} ($\boldsymbol{TE_h^1}$ (130, 310) and $\boldsymbol{TE_h^2}$ (130, 310)).
The resonant frequency of 11.39 GHz at HOMs TE_{130} and TE_{310} contributes to the formation of two sub-hybrid higher modes $TE_h^1(130, 310)$ and $TE_h^2(130, 310)$. The electric field distribution of sub-hybrid mode $TE_h^1(130, 310)$ in the SIW cavity is shown in Fig. 2a. The hybrid mode can be confirmed from the electric field distribution along the edge of the SIW cavity while a pure TE_{220} mode is distributed along the corners of the SIW cavity[5]. Another way of confirming the hybrid mode is by determining the frequency of hybrid modes from the general microwave resonator theory. The frequency of hybrid TE_{220} mode is 11.2 GHz while the frequency of pure TE_{220} mode is 10.11 GHz. The contour plot of the absolute value of the electric field of TE_{310} mode and TE_{130} mode is shown with $+$ sign indicating the electric field in $+z$ direction (upward) and the $-$ sign indicating the electric field in $-z$ direction (downwards). The combination of '$-+-$ & $+-+$' yields the electric field pattern of the hybrid mode with the minimum electric field at the center. The top view of only the Z-component of the electric field distribution of the TE_{310}, TE_{130}, and $TE_h^1(130, 310)$ is shown as the carpet plot in Fig. 2b. The red colour shows the maximum electric field in $+z$ direction and the blue colour shows the maximum electric field in the $-z$ direction.
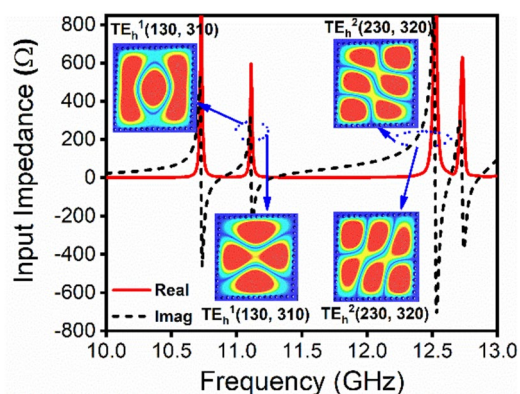

Figure 1. Real and imaginary parts of the input impedance of the SIW cavity representing the two pairs of hybrid higher-order orthogonal modes.
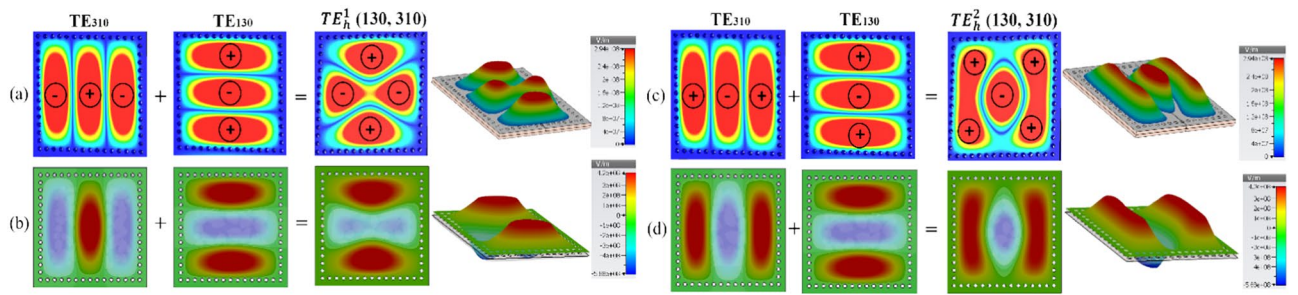
Figure 2. Electric field distribution of TE_h^1 (130, 310) and TE_h^2 (130, 310) (**a**), (**c**) absolute value of electric field, and (**b**), (**d**) z-component of the electric field.

The 3-D view of the TE_h^1(130, 310) mode is also shown. Similarly, the contour and carpet plot of the electric field distribution of the TE_h^2 (130, 310) mode are shown in Fig. 2c,d.

Second hybrid higher-order mode TE_h^1 (230, 320) and TE_h^2 (230,
The second hybrid higher-order modes are formed by the superposition of TE_{230} mode and TE_{320} modes at the resonant frequency of 12.50 GHz. Thus, the two orthogonal modes contribute to the formation of two other sub-hybrid higher modes TE_h^1(230, 320) and TE_h^2 (230, 320). Figure 3a–d show the contour and carpet plot of the electric field distribution of the two sub-hybrid higher modes TE_h^1(230, 320) and TE_h^2 (230, 320), respectively.

Design formulation for radiation null reduction

The method of null reduction commences with the assumption that a pair of multiple slots can be considered same as an array of several antenna elements. The radiation pattern of an antenna radiating in the broadside direction can be represented by the expression[16]:

$$E(u) = \sum_{a=-\infty}^{a=+\infty} (-1)^{a(N-1)} E_a(u) \tag{1}$$

where, N is the total number of array elements (or slots). The center of the array (or slots) is considered at the origin. Also, the total length of the array is normalized to 1. Thus,

$$E_a(u) = \frac{1}{2} \int_{-1}^{1} A(x) \frac{dy}{dx} e^{-j\varphi(x)+jux+jaN\pi y} dx \tag{2}$$

$$= \frac{1}{2} \int_{-1}^{1} A(y) e^{-j\varphi(y)+jux(y)+jaN\pi y} dy \tag{3}$$

where, $u = \frac{kL}{2} sin\theta$, L = aperture length, k = wave number = $\frac{2\pi}{\lambda}$, $A(x)$, $A(y)$ are the amplitude of the current and φ is the phase of the current. $x(y) = \frac{2d(n)}{L}$ where n is the nth element of the array (or n^{th} slot), $d(n)$ is the distance of the nth element from origin. $y(x)$ = source number function in normalized form.

When the structure is symmetric about the origin, then the above equations (2) and (3) can be rewritten as:

$$E_a(u) = \int_{0}^{1} A(x) \frac{dy}{dx} e^{-j\varphi(x)+jux+jaN\pi y} dx \tag{4}$$
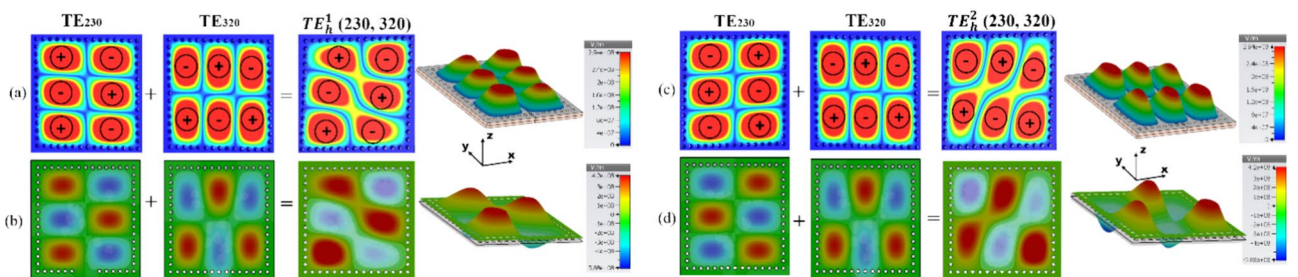

Figure 3. Electric field distribution of TE_h^1 (230, 320) and TE_h^2 (230, 320) (**a**), (**c**) absolute value of electric field, and (**b**), (**d**) z-component of the electric field.

$$= \int_0^1 A(y)e^{-j\varphi(y)+jux(y)+jaN\pi y}dy \tag{5}$$

The values of $A(x) = A(y) = 1$ and $\varphi(x) = \varphi(y) = 0$ for an uniformly excited array. Therefore, Eqs. (2) and (3) can be modified as:

$$E_a(u) = \frac{1}{2}\int_{-1}^1 \frac{dy}{dx}e^{jux+jaN\pi y(x)}dx \tag{6}$$

$$= \frac{1}{2}\int_{-1}^1 e^{jux(y)+jaN\pi y}dy \tag{7}$$

Also, if the spacing is equal, $y(x) = x(y), dy = dx$, but if the spacing is unequal then

$$y(x) = x(y) + f(x) \tag{8}$$

$$x(y) = y(x) + g(y) \tag{9}$$

where, $f(x)$ and $g(y)$ represent the inequality factor. Since $y(x)$ and $x(y)$ offer unique solution and are symmetrical about the origin, therefore they can be considered as odd functions. Subsequently, $f(x)$ and $g(y)$ are also considered as odd. Thus, $f(x)$ and $g(y)$ are represented as Fourier series.

$$f(x) = \sum_{k=1}^\infty r_k \sin k\pi x \tag{10}$$

$$g(x) = \sum_{k=1}^\infty s_k \sin k\pi y \tag{11}$$

On proceeding with the single term of Eqs. (10) and (11), Eqs. (8) and (9) can be expressed as:

$$y = x + \frac{2A_1}{\pi}\sin\pi x \tag{12}$$

$$x = y + \frac{2A_2}{\pi}\sin\pi y \tag{13}$$

Since $dy = dx$; $dy/dx = dx/dy = 1$; therefore, $\left|\frac{df(x)}{dx}\right| \leq 1$ and $\left|\frac{dg(y)}{dy}\right| \leq 1$. Thus, from Eqs. (12) and (13), $|A_1|, |A_2| < \frac{1}{2}$[17]. A positive value of A_1 makes the array elements (slots) near the origin to be denser than at the ends and vice versa. These expressions of the spacing between the array elements (or the multiple slots) yield the best possible radiation performance. On substituting the Eqs. (12) and (13) in Eqs. (6) and (7) The value of A_1 controls the radiation nulls and the side lobe levels. Thus,

$$E(u) = E_0(u) + \sum_{a=1}^{a=+\infty} (-1)^{a(N-1)} G_{-a}(u) \tag{14}$$

where, $G_{-a}(u)$ is a factor of A_1.

If $|A_1| < \frac{1}{6}$ then there is no overlap between two consecutive side lobes[17]. So, the formulation for deciding the unequal spacing between the array elements (slots) as shown in Fig. 4 is summarized in the following steps:

Let N is the number of slots chosen, L is the total aperture length,

1. The position of each slot is given by $d_n = \frac{L}{2}x_n$
2. The value of x_n is $y_n = x_n + \frac{1}{3\pi}\sin\pi x_n$
3. When the structure is considered symmetrical across the origin, then $y_n = \frac{2n}{N}$
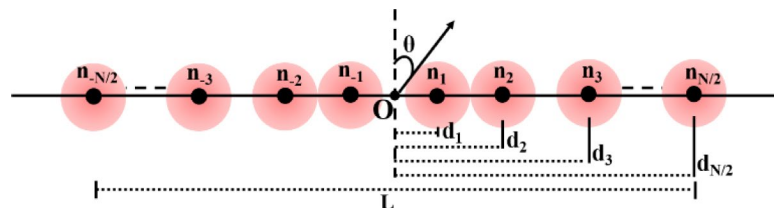

Figure 4. Arrangement of multiple slots positioned at unequal spacing.

The design steps for improved radiation performance for a wideband antenna are summarized as:

1. Start by choosing the highest frequency (f_h) of operation and choosing N.
2. The minimum spacing of the slot from the origin (center) is approximated by $\frac{\lambda_h}{2} = \frac{3}{4} d_{avg}$, where λ_h is the wavelength at highest frequency, d_{avg} is the average spacing between the slots.
3. The aperture length L is determined from the expression: $d_{avg} = \frac{L}{N-1}$

Position of slots for radiating element: example
The estimation of the position of the radiating slots begins with the designing of three configurations of slots (i) two equally spaced slots ($N = 2$, ESS), proceeding to (ii) four equally spaced slots ($N = 4$, *ESS*), and concluding the final design at (iii) four unequally spaced slots ($N = 4$, USS). The slots and their positions are considered symmetrical about the origin. Initially, the general spacing between the two slots is considered to be half wavelength [18]. In Fig. 5a the position of two equally displaced slots from the center contributing to a total separation of $L=0.52\lambda_g$ are shown; where λ_g is determined from the dominant mode frequency of the SIW cavity. Further, the effect of increase in the factor N is studied by positioning them at equal distances in Fig. 5b and at unequal distances in Fig. 5c. However, the total distance of $0.52\lambda_g$ is kept unchanged.

In the arrangement with $N = 4$, and ESS, the four slots are positioned at an equal spacing of $L/(N-1) = L/3 = 0.173\lambda_g = L_{avg}$ with the value of L unchanged. . Conversely, in the arrangement of the $N = 4$, and USS, an unequal spacing between the four slots is determined by the formulation:

Let the number of slots be $N= \{n_1, n_2, n_3, n_4\ldots\ldots, n_N\}$; spacing between the adjacent slots is defined by using the arithmetic progression scheme as Ln_{ij}, where $i = n_1, n_2,\ldots\ldots, n_{N-1}$ and $j= n_2, n_3,\ldots\ldots, n_N$. Thus the total slot array length when N is an even number as:

$$L = (N - 1)L_{n_{\frac{N}{2},\frac{N}{2}+1}} + (N - 2)\Delta L \tag{15}$$

However, when the distribution of slots is symmetric across the origin then, $N = \left\{n_{-\frac{N}{2}}, n_{-\frac{N}{2}+1}, \ldots, n_{-1}, n_1, \ldots, n_{\frac{N}{2}-1}, n_{\frac{N}{2}}\right\}$; spacing between adjacent slots is $L_{n_{ij}}$, where $i = n_{-\frac{N}{2}}, \ldots\ldots n_{\frac{N}{2}-1}, and j = n_{-\frac{N}{2}+1}, \ldots\ldots n_{\frac{N}{2}}$. The total array length will be defined as:

$$L = (N - 1)L_{n_{-1,1}} + (N - 2)\Delta L \tag{16}$$

The value of $L_{n_{-1,1}}$ can be determined by considering two cases:
1. When the distance two central elements is kept less than the average distance ($L_{avg}= 0.173\lambda_g$):

$$L_{n_{-1,1}} < L_{avg}$$

2. When the distance two central elements is kept greater than the average distance ($L_{avg}= 0.173\lambda_g$).
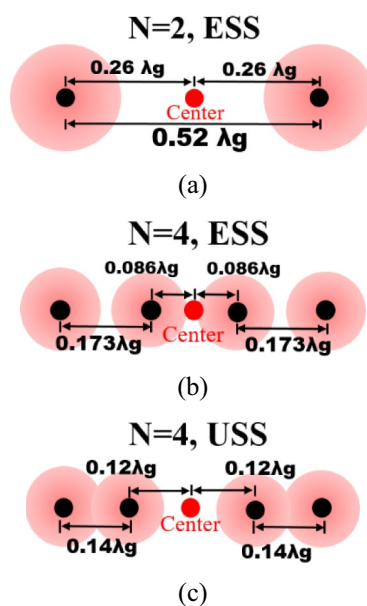
$$L_{n_{-1,1}} > L_{avg}$$

Figure 5. Position of center of the two-slot array and four-slot array with spacing between consecutive slots at Port-1 (**a**) $N = 2$, ESS, (**b**) $N = 4$, ESS, and (**c**) $N = 4$, USS.

Here, the second case where the gap between the two central elements greater than the average distance ($L_{avg} = 0.173\lambda_g$) is considered in the example. The value of ΔL is negative when the slots are densely distributed near the ends than at the center, and ΔL is positive when the slots are densely distributed near the center than at the ends. Thus, the equation to determine the distance between the two central elements in unequally spaced slots case is expressed as:

When $|N|=4$ i.e. $N=\{ n_{-2}, n_{-1}, n_{+1}, n_{+2} \}$ as shown in Fig. 5c then

$$L = 3 * L_{n_{-1,1}} - 2 * \Delta L \tag{17}$$

where, the correction factor $\Delta L < \frac{1}{6}$ so that there is no overlap between two consecutive side lobes[17]. On substituting the value of $\Delta L = 0.1$, and $L = 0.52\lambda g$, we achieve the value of $L_{n_{-1,1}} = 0.24\lambda_g$. This value can be expressed as $L_{n_{-1,1}} = 0.12\lambda_g + 0.12\lambda_g$ (the distance between the two central slots equally displaced from the centre).

Apart from reducing the radiation nulls, proper adjustment of $L_{n_{-1,1}}$ also gives flexibility in choosing the bandwidth of the antenna. If wideband performance is desired then, the minimum centre-to-centre spacing is determined by choosing $\Delta L < \frac{1}{6}$. For narrow band performance $\Delta L \approx \frac{1}{2}$.

Design of multi-slot radiating element for a dual polarized antenna with unequal slot spacing and dual SIW cavity modes

The design of the SIW based dual polarized antenna is discussed in light of the hybrid HOMs and the unequally spaced slots. Dual orthogonal microstrip feed lines are utilized to excite the SIW cavity due to their simple design, easy fabrication, easy matching by controlling the inset position, and easy generation of higher-order modes. The occurrence of the radiation null and the side lobes is minimized by positioning the slots with unequal spacing (as discussed in previous section). So, initially, the radiation performance of the antenna with $N = 2$, ESS and with $N = 4$, ESS is analysed. Later on, the radiation performance is improved with $N = 4$, USS.

N = 2, equally-spaced slots
The two hybrid HOMs are excited initially by loading the SIW cavity with the two rectangular slots at positions discussed in previous section. As a dual polarized antenna is being designed therefore two vertical rectangular slots and two horizontal rectangular slots are positioned at $0.52\lambda_g$ spacing to generate vertical linear polarization (VLP) and horizontal linear polarization (HLP). All these slots together can be realized as a square ring-shaped slot (Fig. 6a) is positioned at the center of the SIW cavity. The slot length can be derived using the conventional square ring slot antenna theory[19]

$$f_l = \frac{c}{(x_1 + x_2)} \left(\sqrt{\frac{\varepsilon_r + 1}{2\varepsilon_r}} \right) \tag{3}$$

where c is the speed of light in free space and f_l is the fundamental mode frequency (SIW cavity), x_1 and x_2 are the inner and outer dimensions of the square ring slot, respectively. The two orthogonal hybrid HOMs help to excite dual linear polarization (DLP): VLP and HLP. The geometrical design variables of the square ring shaped slot are length of slot (x_1) = 22.5 mm, and the width of slot (w_x) = 1.0 mm. The two horizontal rectangular slots (along the x-axis) allow the in-phase superposition of EM waves in the far field when excited from Port-1 only (HLP). Similarly, the two vertical rectangular slots (along the y-axis) allow the in-phase superposition of EM waves in the far field when excited from Port-2 only (VLP). The in-phase superposition enhances the gain of the antenna[20]. However, the two vertical rectangular and the two horizontal slots have opposite phases when individually excited from Port-1 and Port-2, respectively, which leads to inferior radiation performance. Thus, the effective radiation is generated from the pair of horizontal and vertical slots when excited from Port-1 and Port-2, respectively (DLP). Since the two horizontal slots are positioned perpendicular to the surface currents on the top conducting layer, maximum power is radiated from them when excited from Port-1. Similarly, when the antenna is excited from Port-2, maximum power is radiated from two vertical slots as now these two slots
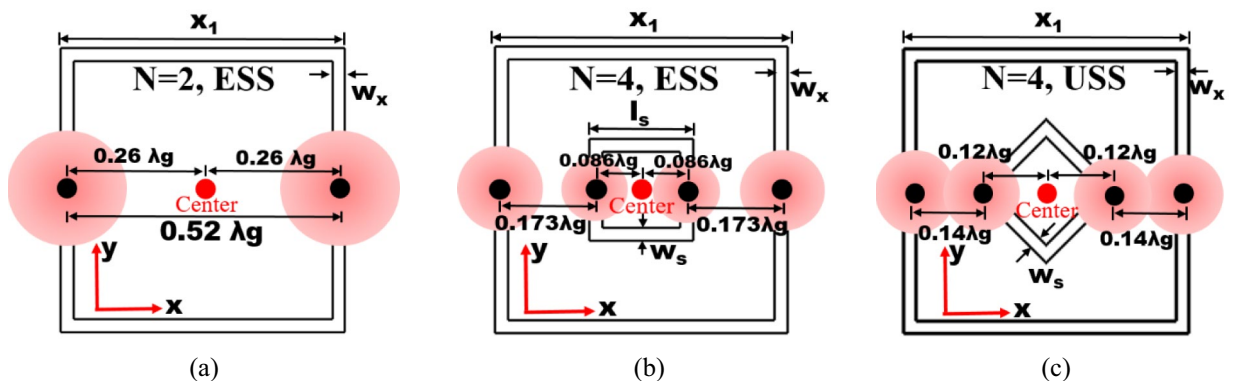

Figure 6. Radiating slots (**a**) ($N = 2$, ESS), (**b**) ($N = 4$, ESS), and (**c**) ($N = 4$, USS).

become perpendicular to the surface currents. Figure 7 explains the in-phase superposition of the DLP antenna with $N = 2$, ESS. Figure 8 shows the two horizontal and two vertical slots positioned inside the SIW cavity.

Antenna (N = 2, ESS) performance
Figure 9 shows the reflection response, isolation, and realized gain of the antenna (only a single square ring slot is implemented). The antenna exhibits 2.0% (11.18–11.50 GHz) bandwidth with center frequency of 11.39 GHz and 8.0% (12.0 –13.0 GHz) with center frequency of 12.58 GHz and isolation >15 dB, with rather inferior impedance matching. However, the gain is 8.9 dBi at 11.39 GHz and 8.37 dBi at 12.58 GHz. To enable further improvement of antenna performance, another square ring-shaped slot is etched inside the main (outer) square ring slot, thereby making the two slots homocentric.
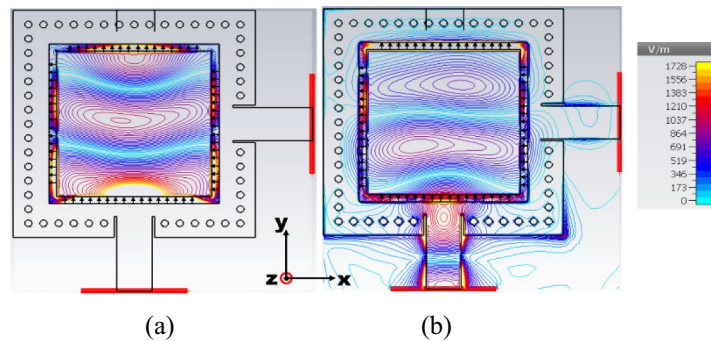
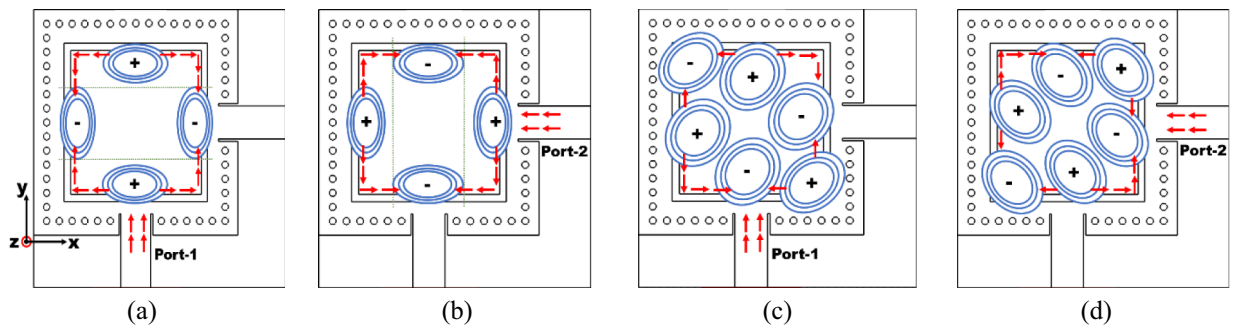**Figure 7.** Electric field isolines of antenna with only single square ring-shaped slot at (**a**) 11.39 GHz, and (**b**) 12.58 GHz.

Figure 8. Electric field, magnetic field distribution and surface currents at (**a**) 11.39 GHz Port-1, (**b**) 11.39 GHz Port-2, (**c**) 12.58 GHz Port-1, and **d** 12.58 GHz Port-2. The H-field distributions, surface currents and the radiating slots are represented by blue, red, and black lines, respectively. The electric field orientation is represented by the + and − signs in the +z and −z directions, respectively.
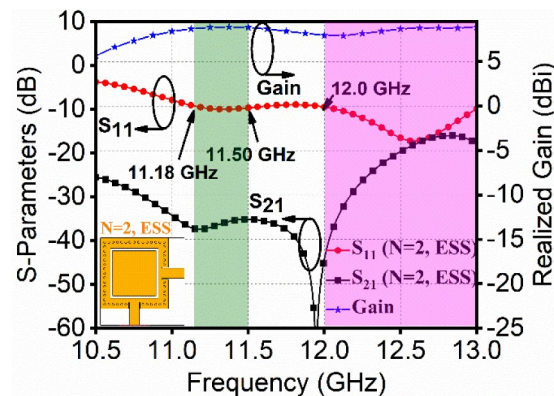

Figure 9. Antenna with $N = 2$, ESS: S-parameters and variation of gain versus frequency.

N = 4, equally-spaced slots

In order to position four equally spaced horizontal and vertical slots, two homocentric square rings slots are utilized as shown in Fig. 6b. The size of the inner square ring slot is decided by considering the effects from fringing fields and theory for cavity model of a microstrip patch antenna. The length of patch formed inside the inner square ring slot is also verified using the empirical formula[19]:

$$L_{patch} = 0.32 \frac{\lambda_0}{\sqrt{\varepsilon_r}} \tag{3}$$

where λ_0 is the free space wavelength at 11.0 GHz (TE$_{130}$) and ε_r is the relative permittivity of the substrate. The length of the inner slot is (l_s) = 8.0 mm, width of inner slot (w_s) = 1.0 mm. As a result, all four horizontal and vertical slots are equally spaced by 0.173 λ_g. Similar to antenna with N=2, ESS, the four horizontal slots offer HLP when excited from Port-1 and also allow superposition of EM waves in phase. The four vertical slots offer VLP when excited from Port-2. Since the four horizontal rectangular slots and four vertical rectangular slots serve as a four-point array, therefore the gain of antenna is also enhanced in comparison to the antenna with N=2. Figure 10 shows the in-phase superposition of the antenna with N=4, ESS. The antenna, when excited from Port-1, shows same phase of electric lines in all four horizontal slots at both 11.39 GHz and 12.58 GHz. It is because the slots are not crossing the magnetic field, but as observed in the vertical slots, the magnetic field lines are crossing the slots. Also, the orientation of electric field lines in vertical slots are cancelling out each other. Thus, minimum radiation is obtained from vertical slots. Figure 11 shows the orientation of the electric field in the +z and − z directions represented by + and − signs.

Antenna (N=4, ESS) performance

The incorporation of an inner square ring slot leads to an improvement in impedance matching at both ports. However, the antenna radiates at the same resonant frequencies 11.39 GHz (TE$_{130}$) and at 12.58 GHz (TE$_{230}$) covering a wider bandwidth. Further, the isolation level between the two orthogonal ports is also improved within the entire frequency band. The antenna performance is shown in Fig. 12 in terms of the simulated reflection coefficient, isolation, and realized gain. At 11.39 GHz, the gain is enhanced to 9.33 dBi as compared to N=2, ESS featuring a single square ring slot. However, at 12.58 GHz, when excited through Port-1, the current in the horizontal slots is in phase at the two extremes but out of phase at the centre of the slots. Thus, the gain is reduced by a small amount at a higher frequency. The realized gain at 12.58 GHz is 7.8 dBi.
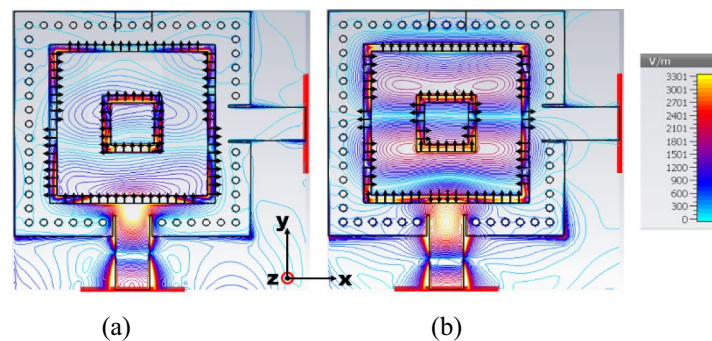

(a)   (b)

Figure 10. Electric field lines and isolines in the xy-plane when excited from Port-1 at (**a**) 11.39 GHz, and (**b**) 12.58 GHz.
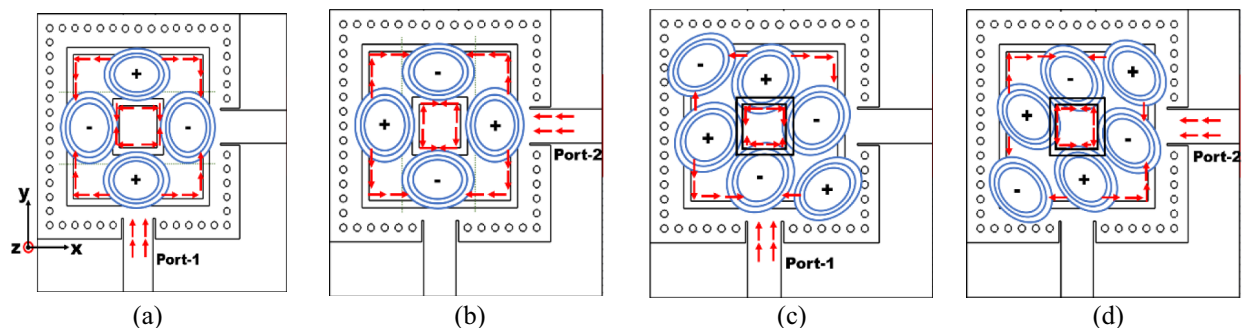

(a)   (b)   (c)   (d)

Figure 11. Electric field, magnetic field distribution and surface currents of antenna with N = 4, ESS at (**a**) 11.39 GHz Port-1, (**b**) 11.39 GHz Port-2, (**c**) 12.58 GHz Port-1, and (**d**) 12.58 GHz Port-2. The H-field distributions, surface currents and the radiating slots are represented by blue, red, and black lines, respectively. The electric field orientation is represented by the + and − signs in the +z and − z directions, respectively.

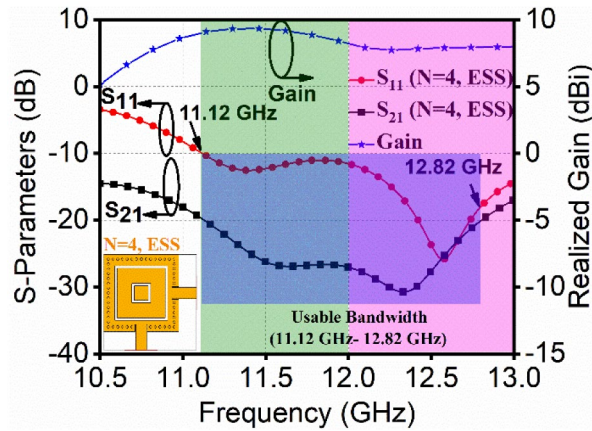**Figure 12.** Antenna (N = 4, ESS): *S*-parameters and variation of gain versus frequency.

N = 4, unequally-spaced slots

Based on the radiating element with *N* = 4, USS as shown in Fig. 6(c), a wide bandwidth enhanced-gain dual linearly polarized antenna with improved isolation is presented here by modifying the spacing between individual slots. The unequal spacing is achieved by rotating the inner square ring slot by 45°. The spacing between the four slots is set to $0.14\lambda_g$, $0.24\lambda_g$, and $0.14\lambda_g$. The dimensions of both slots are kept same in the antenna design with *N*=4, ESS and *N*=4, USS. Rotation by 45° also helps to achieve symmetry along the center. This strategy further improves the impedance matching, thereby offering a wider usable bandwidth and enhanced realized gain. The usable bandwidth is defined as the range of frequencies at which $|S_{11}|$ is below − 10 dB, whereas isolation better than 20 dB. The variation of real and the imaginary parts of input impedance with frequency of SIW cavity, *N*=2, ESS; *N*=4, ESS; and *N*=2, USS has been shown in Fig. 13.

The study illustrates the effect of design modification on the impedance matching at the two hybrid mode frequencies. In *N*=2, ESS, the impedance matching is poor at first hybrid mode (at 11.39 GHz) but as the design advances, the impedance matching is improved. At second hybrid mode, the impedance matching of antenna with *N*=2, ESS and *N*=4, ESS is achieved at 12.58 GHz and for *N*=4, USS it is shifted to 12.35 GHz. The superimposed electric field lines are shown in Fig. 14. At 11.39 GHz when excited through Port-1, the electric field lines of horizontal slots as well as all the four slots of the inner square ring slot are in phase. In *N*=4, ESS only four slots (horizontal or vertical) at an instance were contributing in phase superposition, but in *N*=4, USS a total of six slots (2 horizontal or 2 vertical and 4 slots formed from inner square ring slot) are contributing to in-phase superposition. Thus, an enhanced gain is achieved in *N*=4, USS. Figure 15 shows orientation of the electric field field in the + *z* and − *z* directions represented by + and − signs. Thus, the non-uniform spacing helps to achieve low side lobe levels and to control the phase center along with a controllable main beam of radiation [12,21].

The effect of variation of the distance between the two central elements on the reflection coefficient of the antenna with N = 4, USS is shown in Fig. 16. As the Δ*L* factor increases, the length $L_{n−1,1}$ is also increases and affects the impedance matching between the slot and the feed. When Δ*L* factor is minimum i.e. 0.1, maximum impedance matching is achieved leading to a wider bandwidth.
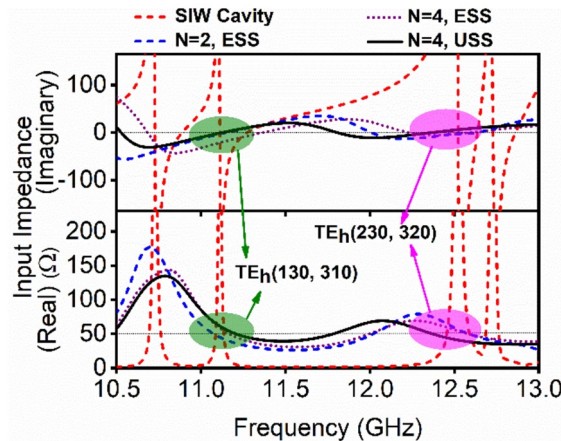

Figure 13. Real and Imaginary parts of input impedance of SIW cavity and antenna with *N*=2, ESS; *N*=4, ESS; and *N*=4, USS illustrating the two hybrid HOMs.
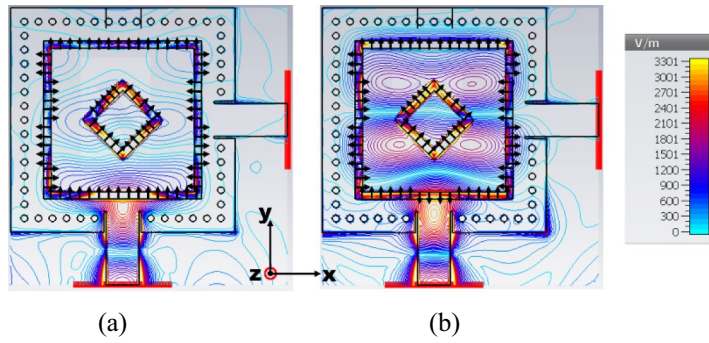
Figure 14. Electric field lines and isolines in the *xy*-plane when excited from port-1 at (**a**) 11.39 GHz, and (**b**) 12.58 GHz.
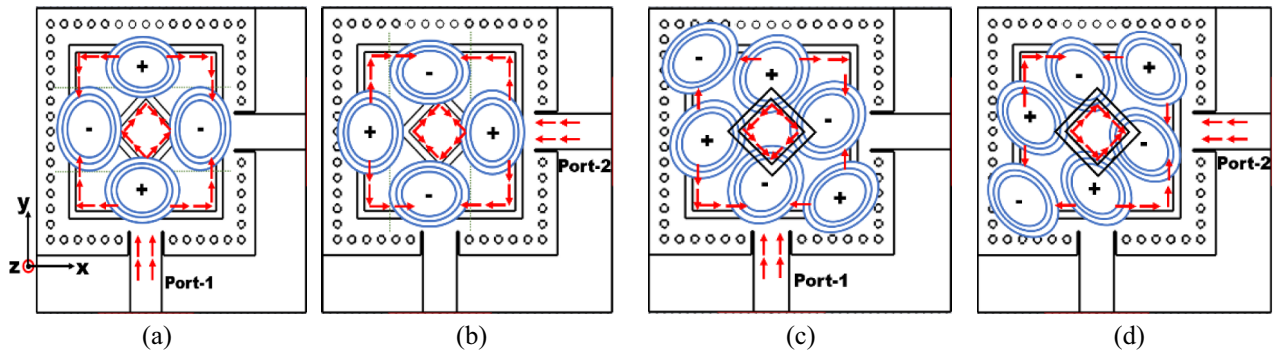

Figure 15. Electric field, magnetic field distribution and surface currents of antenna with $N = 4$, USS at (**a**) 11.39 GHz Port-1, (**b**) 11.39 GHz Port-2, (**c**) 12.35 GHz Port-1, and (**d**) 12.35 GHz Port-2. The H-field distributions, surface currents and the radiating slots are represented by blue, red, and black lines, respectively. The electric field orientation is represented by the + and − signs in the +z and − z directions, respectively.
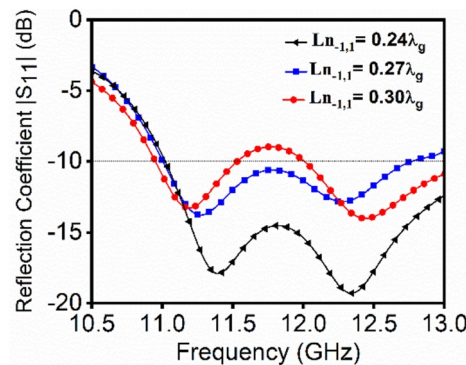

Figure 16. *S*-parameters and gain of antenna (N = 4, USS) as a function of frequency.

Table 1 discusses the main lobe direction, side lobe level at phi-0 and phi-90 and also the phase center (*x,y*) at 11.39 GHz and 12.58/12.53 GHz for $N = 2$, ESS; $N = 4$, ESS; and $N = 4$, USS, respectively. A large reduction in the side lobe level of antenna with $N = 4$, USS can be observed. The main lobe direction and the phase center are at 0° and at (0, 10.35), respectively at 11.39 GHz for $N = 4$, USS; however, at 12.35 GHz the main lobe direction is close to 0°. The condition of symmetry at the center helps to achieve dual polarized response of the antenna. Therefore, maximum permissible main lobe direction and phase center while keeping the dual polarization characteristics intact are achieved by 45° rotation of inner slot as shown in Table 1. Successively, when the inner square ring slot is incorporated, the impedance matching is also improved, which leads to an enhanced bandwidth (11.02-13.5 GHz). The usable bandwidth with minimum 20 dB isolation is 14.5% (11.02-12.75 GHz). The performance of antenna with $N = 4$, USS is depicted in Fig. 17. Due to symmetry of the structure, we have $|S_{11}| = |S_{22}|$ and $|S_{12}| = |S_{21}|$). At 11.39 GHz, an enhanced gain of 9.8 dBi is achieved as compared to conventional single slot antenna.

Antenna/freq	11.39 GHz			12.58 GHz/12.35 GHz		
	Main Lobe dir @ Phi 0/90	Side lobe level @ Phi 0/90	Phase center (x,y)	Main Lobe dir @ Phi 0/90	Side lobe level @ Phi 0/90	Phase center (x,y)
$N=2$, ESS	4°/0°	− 1.2 dB/ − 5.6 dB	3.75, − 1.42	5°/20°	− 14.4 dB/ − 1.50 dB	3.75, 16.6
$N=4$, ESS	359°/0°	− 16.6 dB/ − 6.0 dB	− 0.10, − 1.77	342°/18°	− 15.5 dB/ − 2.10 dB	0.11, 9.85
$N=4$, USS	0°/0°	− 17.8 dB/ − 6.8 dB	0.0, 0.9	5°/15°	− 19.7 dB/ − 10.3 dB	0.0, 10.35

Table 1. Radiation properties of the antenna with $N=2$, ESS; $N=4$, ESS; and $N=4$, USS at the two frequencies.
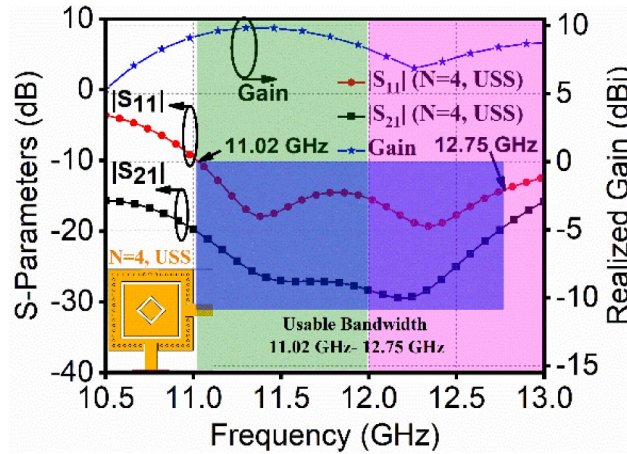

Figure 17. S-parameters and gain of antenna (N = 4, USS) as a function of frequency.

Similar to antenna with $N=4$, ESS at 12.35 GHz when excited through Port-1 the current in the horizontal slots is in phase at the two extremes but out of phase at the centre of the slots. Thus, the gain is reduced by a small amount. The realized gain at 12.35 GHz is 7.15 dBi.

Radiation performance

The normalized simulated radiation patterns of antenna $N=2$, ESS; $N=4$, ESS; and $N=4$, USS, are shown in Fig. 18. The unidirectional pattern is observed with low cross-polarization. However, as the antennas are radiating at two hybrid higher-order modes, the radiation pattern at these two frequencies becomes unstable. Due to these higher-order modes, the antennas exhibit a more complex electric field distribution as compared to the fundamental mode, which result in radiation nulls. These nulls occur due to constructive and destructive interference of the radiated fields from different parts of the slot. The nulls occur at angles where the radiated fields from different parts of the slot interfere destructively, resulting in a cancellation of radiation in those directions. A large radiation null is observed in the far-field pattern of the antenna with $N=2$, ESS in the *yz*-plane
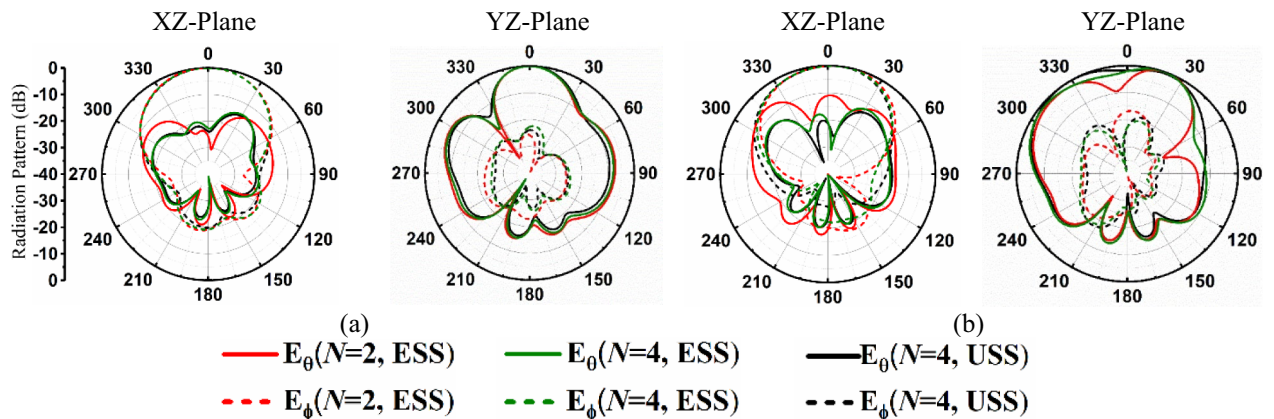

Figure 18. Normalized radiation pattern of antenna with $N=2$, ESS; $N=4$, ESS; and $N=4$, USS when excited from Port-1 at (**a**) 11.39 GHz, and (**b**) 12.58/12.35 GHz.

at both frequencies. However, in $N = 4$, ESS and $N = 4$, USS, the radiation nulls are reduced successively because of increase in N and unequal spacing. The radiation nulls in $N = 2$, ESS are observed at 325° at the frequency of 11.39 GHz and at 59° and 348° at 12.58 GHz. Therefore, with $N = 4$, ESS phase shifts are introduced and the current distribution is modified at the two hybrid modes. The inner square ring slot introduces constructive interference and adjusts the phase of the electric field at the desired angle. In $N=4$, USS, the rotation of the inner square ring slot further leads to an improvement in the radiation characteristics of the antenna in the desired direction. Fig. 19 illustrates the electric field and its phase along with the enlarged view and the 3D- radiation pattern at the two frequencies 11.39 GHz and 12.58/12.35 GHz for $N = 2$, ESS and $N = 4$, USS, i.e. without and with the inner square ring slot. The radiation null is observed at 325° (11.39 GHz) when the antenna comprises $N=2$, ESS (Fig. 19a, b). The phase of the electric field at 325° is 232° which is modified to 64° on loading an inner square ring slot and rotating it by 45°. This shift in phase causes constructive interference which leads to a reduction in the radiation null. Similarly, at 12.58 GHz radiation null is observed at 59° and 348° (cf. Fig. 19c, d) when only the outer square ring slot is utilized. The phase of the electric field is observed as 352° and 290°, respectively. The loading of the slot with $N=4$, USS modifies the phase to 8° and 280°.

The modified phase for the reduction in the null in radiation is determined by calculating the phase difference for desired constructive interference. Constructive interference occurs when the phase difference between the waves is a multiple of 360°. Phase modification = m × (360°—current phase), where m is an integer. If $m < 1$, then the reduction of the radiation null is poor. Otherwise, if $m \geq 1$, the reduction of the radiation null is good. Therefore, the modified phase at the two frequencies is determined as:

At 11.39 GHz (325°)
Modified phase = $0.5 \times (360° - 232°) = 64.0°$
At 12.58 GHz (59°)
Modified phase = $1.0 \times (360° - 352°) = 8.0°$
At 12.58 GHz (348°)
Modified phase = $4.0 \times (360° - 290°) = 280.0°$

Thus, at 11.39 GHz, the reduction of the radiation null is observed but since $m = 0.5$, the null reduction is inferior. However, at 12.35 GHz, the null reduction is larger as the value of $m =1.0$ and 4.0 at the two angles, respectively. It can be observed from the Fig. 19a the phase of the electric field is almost similar for the two cases—without inner square ring slot and with inner square ring slot at all the angles from 0° to 360° except at 325° (position of null). Therefore, even if a phase compensation is applied to the entire range from 0° to
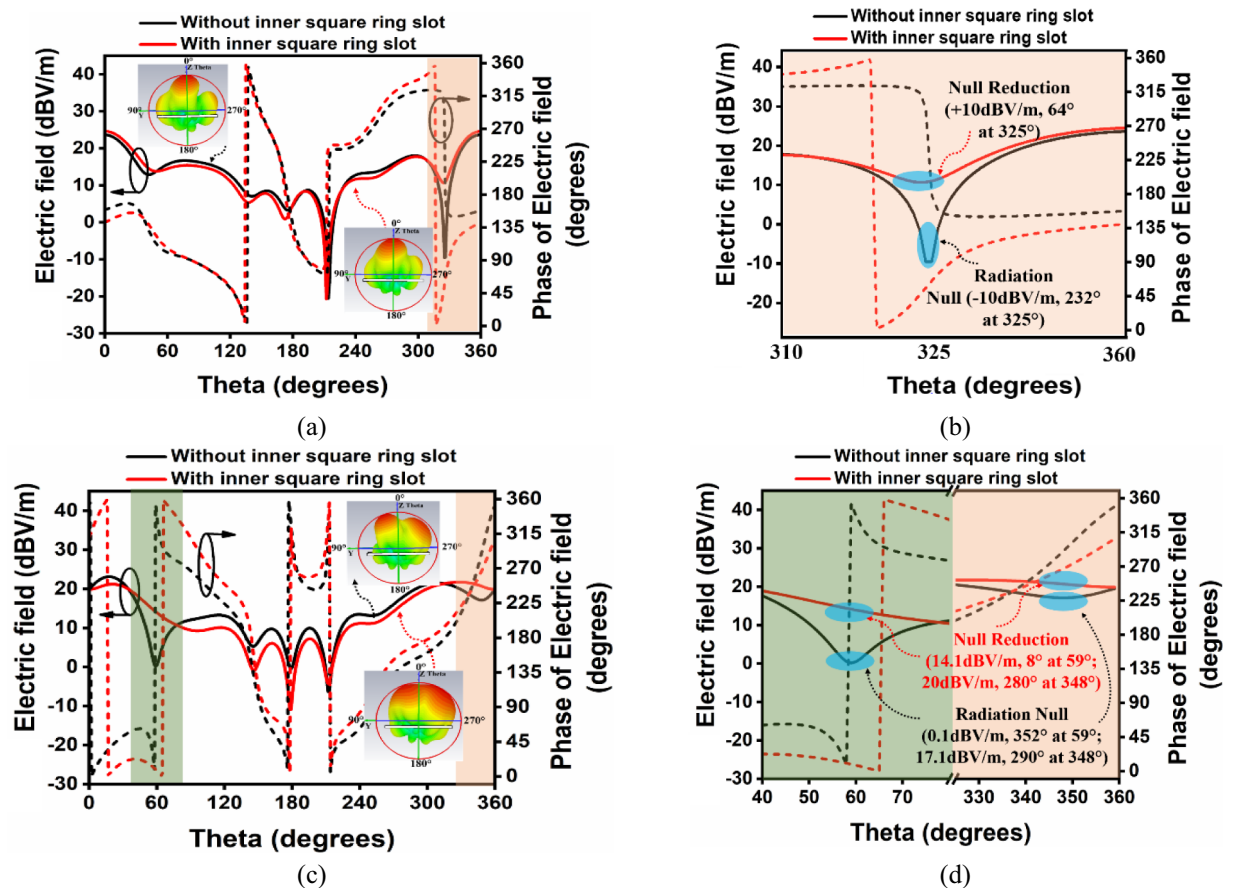

Figure 19. Angular variation of electric field and its phase with its enlarged view and 3D radiation at the two frequencies (**a**), (**b**) 11.39 GHz, and (**c**), (**d**) 12.35 GHz.

360°, no phase difference occurs except at 325°. Thus, only the specific angles with destructive interference are targeted without affecting the radiation pattern at other angles with constructive interference. Figure 20 shows a summarized analysis of the radiation performance of the three antenna designs.

Equivalent circuit model
The step by step process for modelling the equivalent circuit of the dual polarized antenna with $N = 4$, USS begins with the development of equivalent circuit for first hybrid higher order mode, and then second hybrid higher order mode. The entire circuit is designed by following the three concatenated stages: a feeding stage, cavity stage, and a radiation stage. Initially, only the feeding stage and cavity stage are utilized. Subsequently, the equivalent circuit model is developed for the single port excited antenna with $N=2$, ESS; $N=4$, ESS; $N=4$, USS, and finally for dual port excited antenna structure with $N=4$, USS.
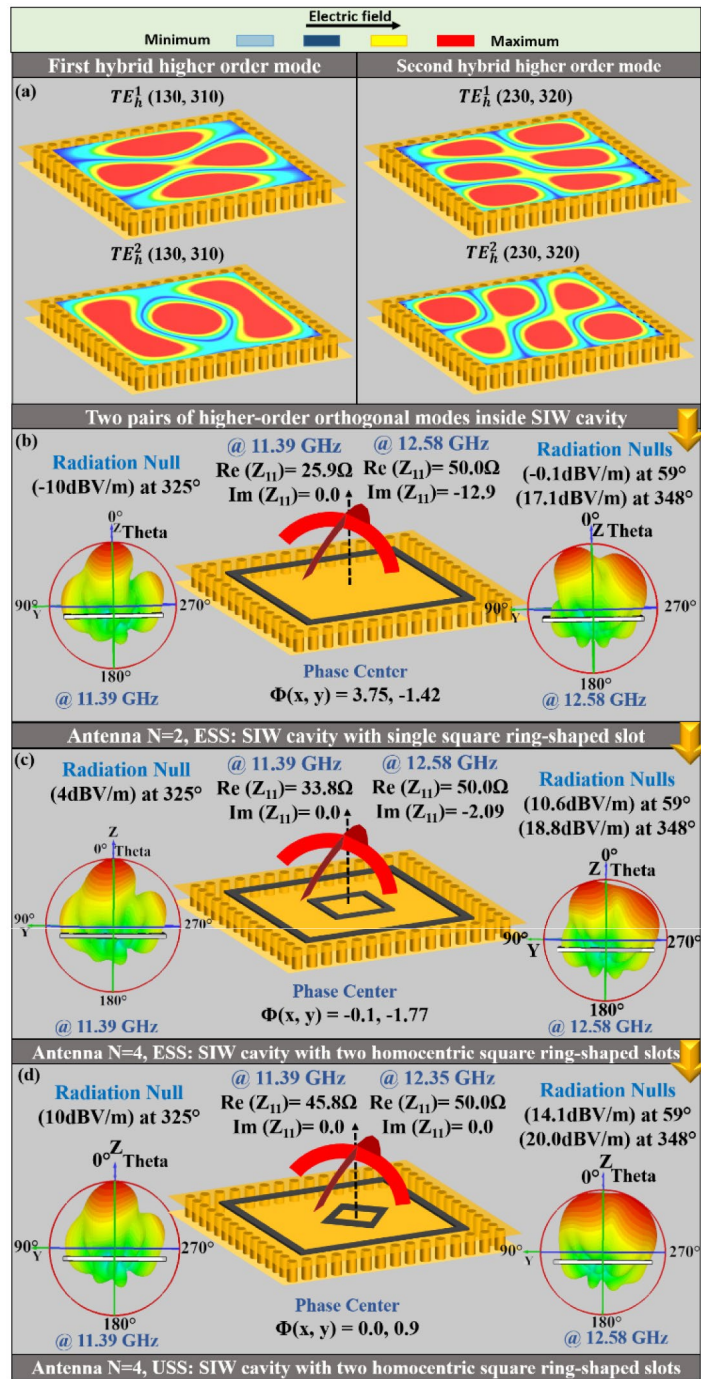

Figure 20. Summarized radiation performance of the three antenna designs.

Figure 21a shows the equivalent circuit model for first hybrid higher order mode in SIW cavity. The microstrip feed is represented by a resistance R_F and the feed-SIW coupling by the transformer T_{mode1}. The cavity stage is modelled by a parallel RLC circuit corresponding to the frequency at mode-1. The component values are: R_F = 2.34 Ω, T_{mode1} = 1.79, R_{mode1} =7.8 kΩ, L_{mode1} =0.347 nH, C_{mode1} =0.55 pF. The frequency response shown in Fig. 21b compares the real and imaginary curves of the input impedance for mode-1 obtained by simulating the equivalent circuit model (ECM) and by CST. Similarly, the equivalent circuit for the second hybrid higher order mode along with its input impedance curves is shown in Fig. 21c, d. The component values are R_F= 0.6 Ω, T_{mode2}= 1.79, R_{mode2}=0.26 kΩ, L_{mode2}=0.386 nH, C_{mode2}=0.428 pF.

The equivalent circuit for mode-1 and mode-2 are combined and used together for modelling the antenna structure with slots. The radiating slots form the third stage termed as the radiation stage. A parallel resonant circuit represented by $PRLC_{outer}$ is modeled for the radiating slot (outer square ring shaped slot) and is coupled to the cavity stage with a transformer that provides SIW-slot coupling. The equivalent circuit for the single port antenna structure with N=2, ESS is shown in Fig. 22a. The component values are R_1=23 Ω; T_{FS}=1.79; $PRLC_{mode1}$=6.7 kΩ, 0.36 nH, 0.55 pF; $PRLC_{mode2}$=0.268 kΩ, 0.38 nH, 0.43 pF; C_1=2.61 pF; L_1=4.6 nH; T_{SS}=1.96; $PRLC_{outer}$= 8 kΩ, 0.762 nH, 0.23 pF. The real and imaginary parts of the input impedance are shown in Fig. 22b. A dual mode response is observed from the figure. Similarly, the equivalent circuit is modeled for the antenna structure with N=4, ESS, and N=4, USS shown in Fig. 22c, e, respectively. The radiation stage comprises two parallel resonant circuits $PRLC_{outer}$ and $PRLC_{inner}$ coupled by a capacitor C_3. The effect of the two is shown in Fig. 22b, f. The component values of antenna structure with N=4, ESS are R_1=8.36 Ω; T_{FS}=1.79; $PRLC_{mode1}$=0.26 kΩ, 0.43 nH, 0.54pF; $PRLC_{mode2}$=3.9 kΩ, 0.38 nH, 0.49 pF; C_1=3.89 pF; L_1=3.0 nH; C_3=0.05 pF; T_{SS}=1.96; $PRLC_{outer}$= 2.4 kΩ, 0.335 nH, 0.50 pF; $PRLC_{inner}$= 5.0 kΩ, 1.21 nH, 0.72 pF. The component values of antenna with rotated square ring slot (N=4, USS) are R_1=11.38 Ω; T_{FS}=1.79; $PRLC_{mode1}$=6.1 kΩ, 0.423 nH, 0.54 pF; $PRLC_{mode2}$=0.28 kΩ, 0.39 nH, 0.55 pF; C_1=1.61 pF; L_1=3.7 nH; C_3=0.05 pF; T_{SS}=1.96; $PRLC_{outer}$= 2.0 kΩ, 0.535 nH, 0.31 pF; $PRLC_{inner}$= 5.5 Ω, 1.21 nH, 0.72 pF. The final equivalent circuit model of the dual polarized antenna with N = 4, USS is shown in Fig. 23a. Two impedance matching transformers T_1 and T_2 are used between the resonator and input signals at Port-1 and Port-2. The coupling between the SIW cavity and the radiating slots is achieved by an ideal transformer T_3. Parallel circuits RLC_3 and RLC_4 represent the two square ring slots separated by a capacitor C_3. Parallel circuits RLC_1 and RLC_2 along with series L_1C_1 elements excite the dual modes of the SIW cavity. The parameters of all the equivalent circuit models are extracted by Keysight Advanced Design System (ADS) software. Table 2 shows the values of the circuit components of the dual polarized N=4, USS antenna. A comparison between the S-parameters of the EM model and the equivalent circuit model (ECM) is depicted in Fig. 23b.

Parametric analysis

Here, a parametric study is carried out to identify crucial dimensions of the antenna structure and their effects on electrical/field characteristics. Fig. 24(a) illustrates that the width of the outer square ring-shaped slot w_x plays an important role in the improvement of the impedance bandwidth; however, this parameter has little effect on the port isolation. The increase in the length of the outer square ring slot x_1 helps in improving both impedance matching and isolation substantially, as shown in Fig. 24b. This effect is also investigated in the equivalent circuit model, in which the analogous change in response due to a change in outer square ring slot length is translated
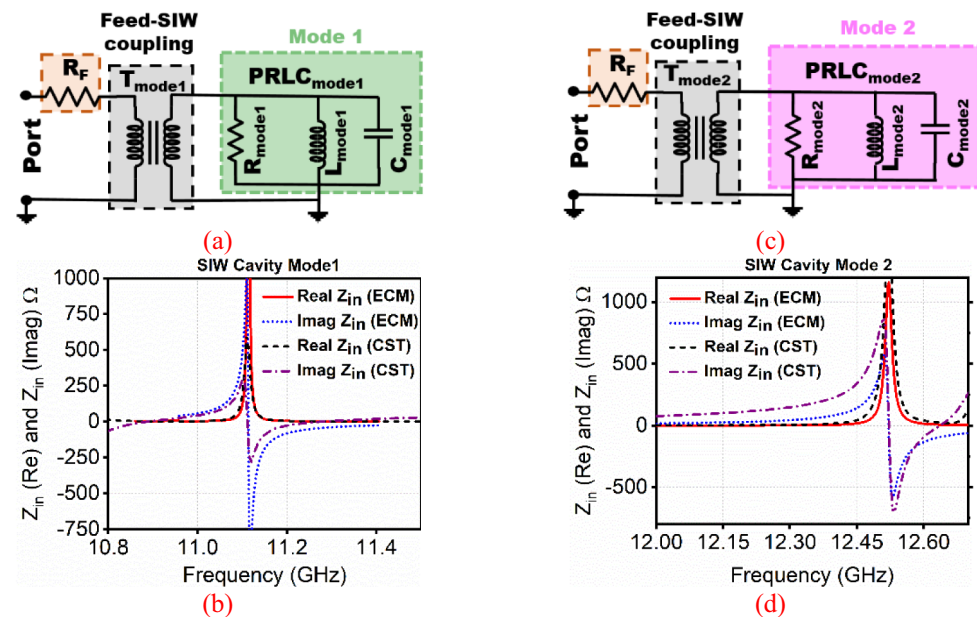

Figure 21. Functional overview of the circuit stages of the first hybrid higher order mode (**a**) equivalent circuit model, and (**b**) input impedance.
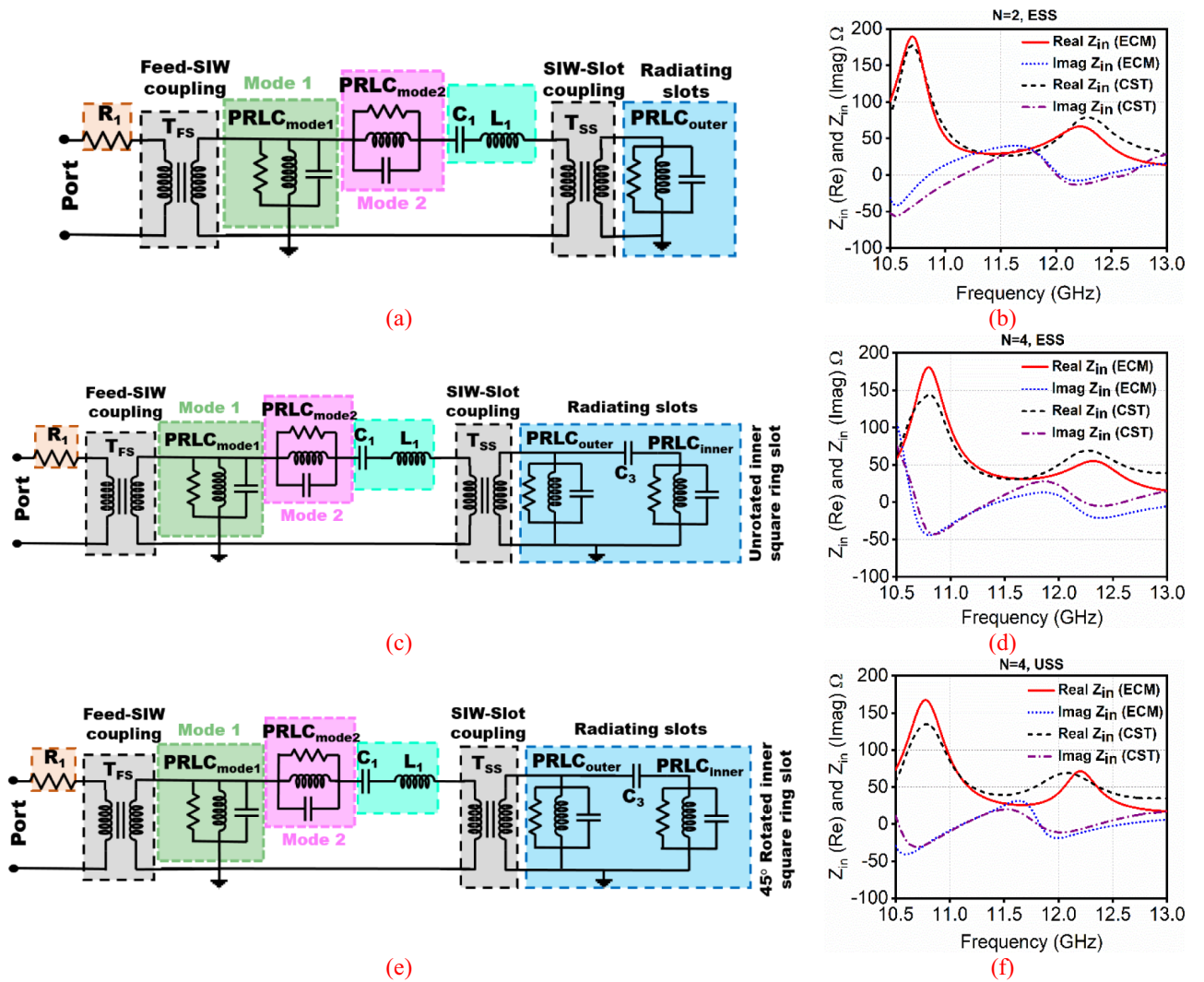
Figure 22. Equivalent circuit model: (**a**) N = 2, ESS, (**c**) N = 4, ESS, (**e**) N = 4, USS; Input impedance of (**b**) N = 2, ESS, (**d**) N = 4, ESS, (**f**) N = 4, USS with single port excitation.
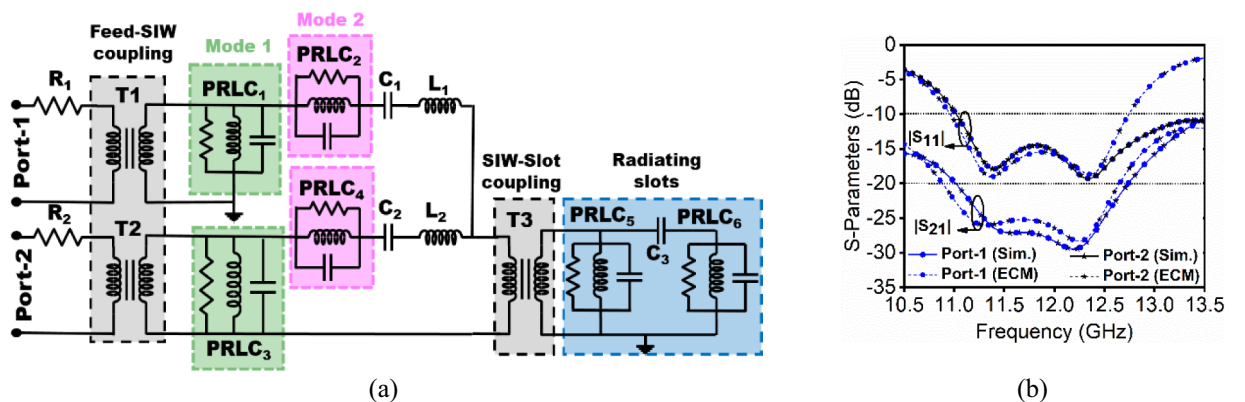

Figure 23. (**a**) Equivalent circuit model (ECM) of the proposed antenna (**b**) comparison between the S-parameters of the EM model and the ECM model.

Component	Value	Component	Value	Component	Value
R_1	9.9Ω		8 KΩ		0.2KΩ
R_2	9.9Ω	$PRLC_1$	0.4 nH	$PRLC_2$	0.39nH
T_1	1.8		0.54 pF		0.55pF
T_2	1.8		8 KΩ		0.2KΩ
T_3	2	$PRLC_3$	0.4 nH	$PRLC_4$	0.39nH
L_1	2.49nH		0.54 pF		0.55pF
L_2	2.24nH		5.4KΩ		1.76KΩ
C_1	0.46pF	$PRLC_5$	0.395nH	$PRLC_6$	0.53nH
C_2	0.46pF		0.55pF		0.72pF
C_3	0.05pF				

Table 2.. Equivalent circuit model parameters.
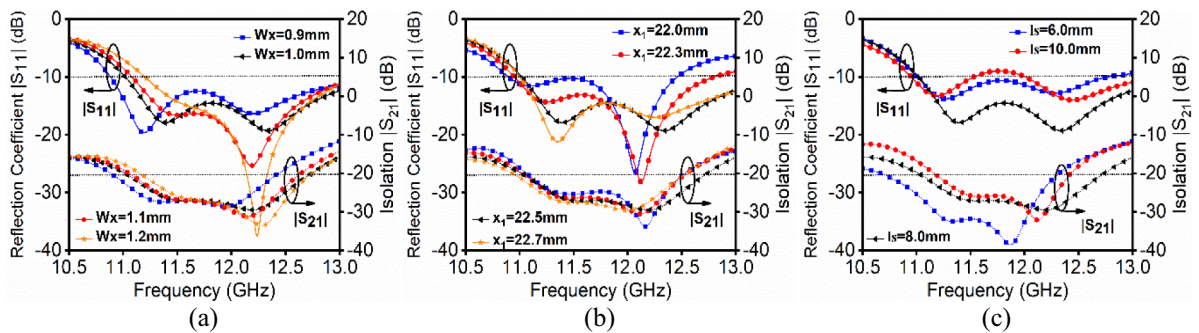

Figure 24. (**a**) Variation in S_{11} and S_{21} as a function the width of the outer square ring slot w_x, (**b**) variation in S_{11} and S_{21} as a function of the length of the square ring slot x1, (**c**) variation in S_{11} and S_{21} as a function of the length of the inner square ring slot l_s.

to circuit parameters; the linear change in the values of L_5 is seen while C_5 remains constant. Similarly, by fixing the inductor L_5 and linearly changing C_5, the variation in bandwidth is noticed. The effect of slot length changes on the component values of L_5 and C_5 has been summarized in Table 3. It has been observed that varying the length l_s of the inner square ring slot has a negligible effect on the resonant frequency; however, the impedance matching and isolation decreases as the slot length increases, which is shown in Fig. 24c. This variation affects the coupling between the SIW cavity and the concentric slots. The highest impedance bandwidth with an improved reflection coefficient is achieved when $l_s = 8$ mm with acceptable isolation between the two ports. This effect can be mapped to the equivalent circuit model: a corresponding change L_1 component is observed. Table 4 shows the effect of variation in inner slot length on the values of L_1, keeping other components fixed.

Design guidelines
The design guidelines for a SIW based dual polarized antenna with reduced radiation nulls based on the unequally spaced slot strategy are formulated below:

> *Step 1* Choose the desired frequency and the orthogonal mode. Here, *f*=11.2 GHz, and orthogonal modes TE_{130}/TE_{310} are selected.

		Circuit Model		EM analysis
		$C_5 = 0.55$pF (Fixed)	$L_5 = 0.395$nH (Fixed)	Geometrical parameter
Resonant frequencies (GHz)	Corresponding change in usable BW(GHz)	L_5 (nH)	C_5 (pF)	x_1 (mm)
11.05, 12.05	11.10–12.5	0.374	0.532	22.0
11.25, 12.10	11.10–12.5	0.381	0.541	22.3
11.39, 12.35	11.02–12.75	0.395	0.55	22.5
11.3, 12.3	11.02–12.5	0.402	0.559	22.7

Table 3. Effect of variation of outer square ring slot length.

Resonant frequency (GHz)	Corresponding change in S_{11} (dB)	Circuit Model L_1 (nH)	EM analysis Geometrical parameter l_s (mm)
11.25, 12.25	− 13.2, − 12.55	2.32	6
11.39, 12.35	− 18, − 19.5	2.49	8
11.25, 12.45	− 13, − 14.3	2.12	10

Table 4. Effect of variation of inner square ring slot length.

Step 2 Design a square-shaped SIW cavity with dimension *1.6 λ_g × 1.6λ_g*, where λ_g is calculated for the orthogonal modes TE$_{130}$/TE$_{310}$ at 11.2 GHz.
Step 3 Design two 50 Ω orthogonal microstrip feedlines to excite the SIW cavity-backed antenna structure.
Step 4 Choose the number of rectangular slots to be loaded in the SIW cavity. Here, *N=4*.
Step 5 Position the four unequally spaced rectangular slots with consecutive gaps of *0.14 λ_g, 0.24 λ_g, and 0.14 λ_g*, between them, where λ_g is calculated for dominant mode TE$_{110}$ at 4.95 GHz.
Step 6 Place the four rectangular slots horizontally as well as vertically forming two concentric square ring-shaped slots.
Step 7 Based on the gap, the length of the outer square-ring-shaped slot is calculated (0.14+0.24+0.14+0.024) λ_g and the length of inner square-ring-shaped slot is (0.24+0.024) λ_g.
Step 8 Rotate the inner square ring slot along *z*-axis by an angle 45°. This rotation creates unequal spacing between the slots.
Step 9 Analyse the input impedance of the antenna. At the resonance, the impedance matching should be 50 Ω which can be optimized by tuning the inset in the microstrip feed.
Step 10 Check the isolation, which should be more than 20 dB. Also, analyze the radiation pattern to ensure it does not have nulls.
Step 11 Validate the antenna performance by developing an equivalent circuit model, as well as by prototype measurements.

Results
Fabrication and experimental validation
The antenna is fabricated on RT/Duroid 5870 substrate (ε_r = 2.33, tanδ = 0.0012) of thickness 1.57 mm. The prototype of the SIW-based dual polarized antenna has been fabricated and shown in Fig. 25a. The fabricated antenna is tested using the vector network analyzer (E5071C). The corresponding resonating modes occur at the frequencies 11.4 GHz and 12.3 GHz. The comparison between the simulated and measured *S*-parameters is shown in Fig. 25b. At the resonant frequency, the measured isolation between the ports is 28.8 dB at 11.4 GHz and 30.2 dB at 12.3 GHz. The measured bandwidth for which the $|S_{11}|$ and $|S_{22}|$ are less than − 10 dB is 14.46% (10.9 GHz to 12.60 GHz). The radiation pattern of the antenna is measured in two orthogonal planes (in θ = 0˚(*xz*) and θ = 90˚(*yz*) planes) at frequencies 11.4 and 12.3 GHz. The far-field measurement setup inside an anechoic chamber is shown in Fig. 25c. A dual-ridge horn antenna DRH 20 mounted on a fixed table is utilized at the receiver end. However, the antenna under test (AUT) is mounted on the rotating table. The comparison between the measured and simulated broadside radiation patterns has been shown in Fig. 26a–d. The antenna exhibits the dual linearly polarized radiation in the orthogonal planes. The ratio of co-polarization to cross-polarization level in the direction of maximum radiation is less than − 20 dB. The agreement between the measured and simulated radiation patterns is satisfactory. The gain characteristic has been shown in Fig. 25b. The gain reduces at around 12.25 GHz. However, the realized gain measured at 11.4 GHz and 12.3 GHz is 9.5 dBi and 7.85 dBi, respectively. The reason for the decrease in the antenna gain at 12.25 GHz is due to the variation in the impedance matching at 12.25 GHz. This variation leads to a mismatch between the antenna and the feedline thereby reducing the input power delivered to the antenna, and thus lowering the gain. It can be observed from the input impedance graph shown in Fig. 13 that at 12.25 GHz, the real part of the impedance is 60Ω. Overall, the results shown indicates that the proposed antenna has the advantages of enhanced gain, wide bandwidth, improved radiation performance, and compatibility with dual-polarized applications.

Table 5 provides a detailed comparative analysis between the antenna structure proposed in this study and a selection of state-of-the-art higher-order mode-based antennas reported in the recent literature. Antenna designs in [5], [4], [22], [3], [23] offer dual polarization, whereas designs of [24] and [25] offer single polarization. The analysis focuses on key performance metric which is level of broadside radiation nulls, along with other performance parameters that include gain, bandwidth, isolation, and the GSR. GSR, defined as the ratio of antenna gain to its physical size, serves as a pivotal parameter. In this aspect, the proposed technique excels in demonstrating reduction of radiation null along with the highest GSR value, which signifies superior gain per unit area. While all antenna structures listed in the table exhibit noteworthy gains, the proposed design outperforms even the dual-polarized antenna detailed in [3], which boasts maximum gain and isolation but lags behind in terms of GSR. Notably, all of the considered antennas utilizing higher-order modes exhibit radiation nulls in the broadside direction. Here, the novelty and the advantages of the proposed antenna are particularly pronounced as a substantial reduction in radiation nulls is achieved. At 11.4 GHz, the radiation null plunges to an impressive − 12 dB, and at 12.3 GHz, it nearly vanishes, registering at 0.5 dB. Moreover, the proposed antenna also showcases a usable bandwidth of 14.6%, a testament to its wideband performance achieved from dual hybrid HOMs. Thus, by utilizing the
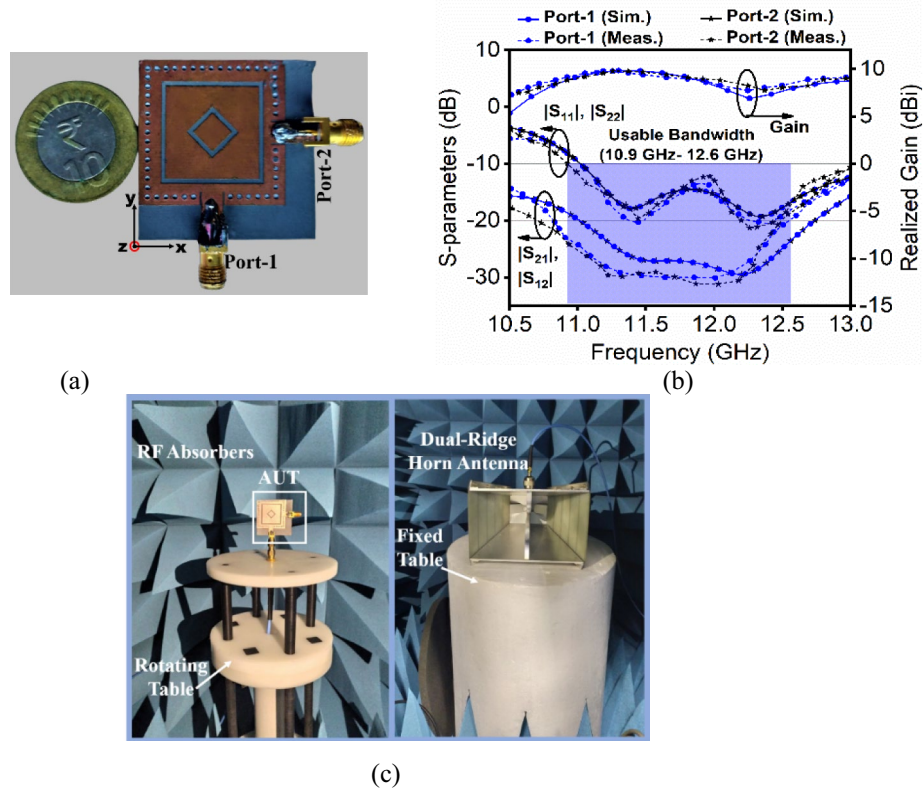
Figure 25. (**a**) Photograph of a fabricated prototype of the antenna, (**b**) comparison between the simulated and measured *S*-parameters of the proposed antenna, and (**c**) far-field measurement setup of the dual polarized antenna.
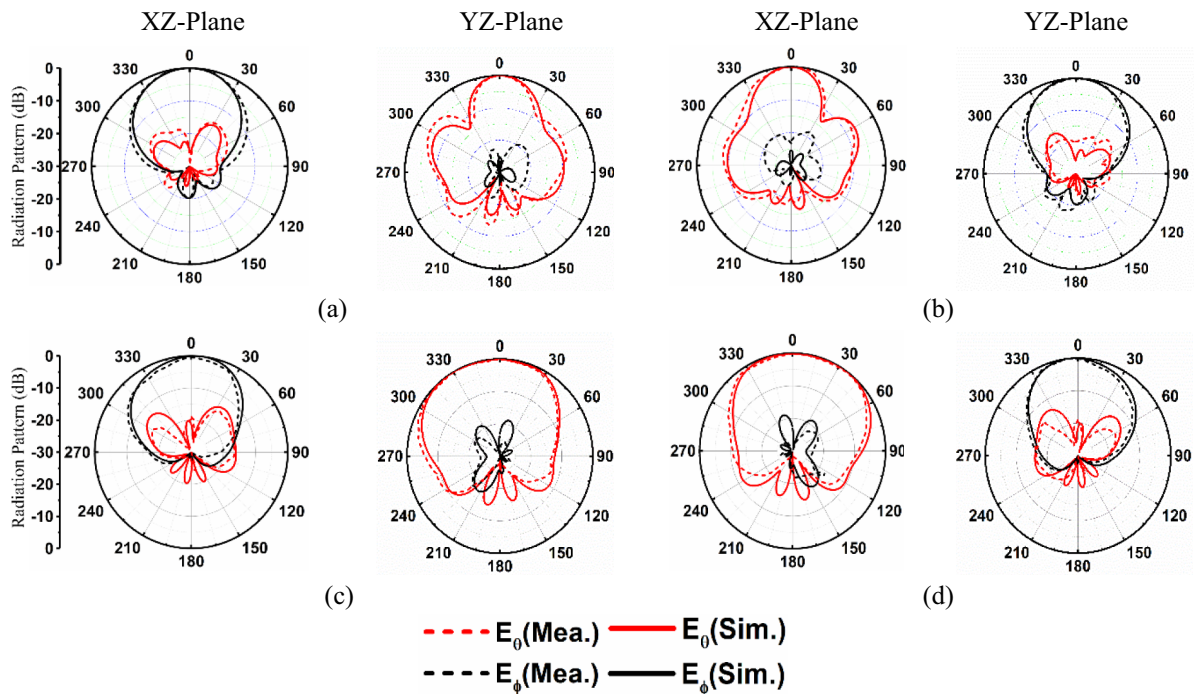

Figure 26. Measured and simulated radiation patterns of the proposed antenna at 11.4 GHz, (**a**) Port-1, (**b**) Port-2; at 12.3 GHz (**c**) Port-1, (**d**) Port-2.

Ref	Freq (GHz)	Gain (dBi)	−10 dB BW (%)	Usable BW (%)	X-Pol (dB)	Isolation (dB)	Size (λ_0^2)	GSR (dBi/λ_0^2)	Broadside radiation nulls E-plane (Port-1)	E-plane (Port-2)	Higher-order modes	Pol
[5]	10.84	10.64	1.56	1.56	−40	30	1.44×1.44	5.13	−30 dB @ 333° −18 dB @ 25°	−35 dB @ 333° −18 dB @ 25°	TE$_{430}$, TE$_{340}$	Dual
[4]	4.8,4.9, 5.0	9.6	6	6	−29	27	1.3×1.3	5.6	−18 dB @ 325° −18 dB @ 35°	−18 dB @ 325° −18 dB @ 35°	TM$_{05}$, TM$_{03}$	Dual
[22]	5.96	11.5	3.0	0	<−20	>14	1.65×1.65	4.22	−30 dB @ 120° −19 dB @ 60°	−30 dB @ 60° −19 dB @ 120°	TM$_{50}$	Dual
[3]	38	14	12.5	12.5	<−20	40	1.67×1.67	5.01	−25 dB @ 60° −25 dB @−60°	−30 dB @ 60° −25 dB @ −60°	TE$_{340}$	Dual
[24]	11.0	15	3.46	N.A	<−20	N.A	π×1.22×1.22	3.17	−25 dB @ 18° −15 dB @ −18°		TM$_{12t\triangleright}$, TM$_{14}$	Single
[25]	18.5	11.5	10.5	N.A	<−18	N.A	π×0.74×0.74	6.68	−15 dB @ 45°		TM$_{31}$, TM$_{12}$	Single
[23]	4.9	12.05	3.87	1.66	<−18	16.5	2.29×2.29	2.29	−40 dB @ 32° −20 dB @ −330°	−40 dB @ 32° −20 dB @ −330°	TM$_{50}$	Dual
This Work	11.4, 12.3	9.5	**16.6**	**14.6**	<−20	**29**	**1.05×1.05**	**8.61**	**−12 dB @ 325° −0.5 dB@348°**	**−12 dB @ 35° −0.5 dB@12°**	TE$_{320}$, TE$_{230}$ TE$_{130}$, TE$_{310}$	Dual

Table 5. Comparison between the proposed design and state-of-the-art HOM based antennas. *GSR:—Gain to size ratio; N.A.:- Not Applicable.*

hybrid HOMs and unequal spacing between multiple slots the dual polarized antenna can be designed to achieve improved radiation performance.

Conclusion

This paper presented a novel technique for designing a single antenna element with improved radiation performance, normally degraded by the use of HOMs. The radiating element of antenna is designed by utilizing several slots that are unequally spaced. The methodology for choosing the unequal spacing is presented and the effects of increasing and decreasing the spacing is also discussed. The unequal spacing helped reducing the radiation nulls, side lobe levels, and adjust the phase center of the antennas. The presented technique is employed to design a wideband (14.6%) enhanced gain (9.5 dBi) SIW based dual polarized antenna by utilizing HOMs and reducing the radiation nulls, side lobe levels and phase adjustment by using the unequally spaced slots. The phase center of the antenna is adjusted from $\phi(x,y) = (3.75, −1.42)$ to $\phi(x,y) = (0.0, 0.9)$ along with a larger reduction in side lobe levels of up to −19.7 dB. Constructive interference, achieved through precise phase differences between electromagnetic waves (a multiple of 360°), reduces radiation nulls in the broadside direction. At the frequency of 12.35 GHz the radiation nulls are almost completely removed while at the frequency of 11.39 GHz a larger significant reduction in nulls is achieved. The aforementioned features make the proposed methodology an exceptional and versatile candidate for development of a variety of high-performance single-element antennas with multiple slots.

Data availability

All Data has been included in study.

References

1. Khan, Q. U. *et al.* Higher order modes: A solution for high gain, wide band patch antennas for different vehicular applications. *IEEE Trans. Veh. Technol.* **66**, 3548–3554 (2016).
2. Wu, P., Liao, S. & Xue, Q. Wideband excitations of higher-order mode substrate integrated waveguides and their applications to antenna array design. *IEEE Trans. Antennas Propag.* **65**, 4038–4047 (2017).
3. Zhao, W., Li, X., Qi, Z. & Zhu, H. High-order-mode cavity fed antenna arrays for diverse polarizations with compact size, high gain, and high efficiency. *IEEE Trans. Antennas Propag.* **70**, 1045–1056 (2021).
4. Luo, Y., Chen, Z. N. & Ma, K. A single-layer dual-polarized differentially fed patch antenna with enhanced gain and bandwidth operating at dual compressed high-order modes using characteristic mode analysis. *IEEE Trans. Antennas Propag.* **68**, 4082–4087 (2019).
5. Li, W., Tang, X. & Yang, Y. Design and implementation of SIW cavity-backed dual-polarization antenna array with dual high-order modes. *IEEE Trans. Antennas Propag.* **67**, 4889–4894 (2019).
6. Han, W., Yang, F., Ouyang, J. & Yang, P. Low-cost wideband and high-gain slotted cavity antenna using high-order modes for millimeter-wave application. *IEEE Trans. Antennas Propag.* **63**, 4624–4631 (2015).
7. Li, W. *et al.* Substrate integrated waveguide cavity-backed slot Array antenna using high-order radiation modes for dual-band applications in $ K $-band. *IEEE Trans. Antennas Propag.* **65**, 4556–4565 (2017).

8. Al-Husseini, M., Yaacoub, E., Baydoun, M. & Ghaziri, H. Independent control of the beamwidth and sidelobe level of Taylor one-parameter arrays. In *2017 Progress In Electromagnetics Research Symposium-Spring (PIERS)* 3335–3339 (2017).

9. de Abreu, G. T. F. & Kohno, R. A modified Dolph-Chebyshev approach for the synthesis of low sidelobe beampatterns with adjustable beamwidth. *IEEE Trans. Antennas Propag.* **51**, 3014–3017 (2003).

10. Zhang, X., Zhu, L. & Wu, Q.-S. Sidelobe-reduced and gain-enhanced square patch antennas with adjustable beamwidth under TM 03 mode operation. *IEEE Trans. Antennas Propag.* **66**, 1704–1713 (2018).

11. Sandler, S. Some equivalences between equally and unequally spaced arrays. *IRE Trans. Antennas Propag.* **8**, 496–500 (1960).

12. King, D., Packard, R. & Thomas, R. Unequally-spaced, broad-band antenna arrays. *IRE Trans. Antennas Propag.* **8**, 380–384 (1960).

13. Harrington, R. Sidelobe reduction by nonuniform element spacing. *IRE Trans. Antennas Propag.* **9**, 187–192 (1961).

14. Deslandes, D. & Wu, K. Accurate modeling, wave mechanisms, and design considerations of a substrate integrated waveguide. *IEEE Trans. Microw. Theory Tech.* **54**, 2516–2526 (2006).

15. Bozzi, M., Georgiadis, A. & Wu, K. Review of substrate-integrated waveguide circuits and antennas. *IET Microw. Antennas Propag.* **5**, 909–920 (2011).

16. Ishimaru, A. Unequally spaced arrays based on the poisson sum formula. *IEEE Trans. Antennas Propag.* **62**, 1549–1554 (2013).

17. Ishimaru, A. & Chen, Y.-S. Thinning and broadbanding antenna arrays by unequal spacings. *IEEE Trans. Antennas Propag.* **13**, 34–42 (1965).

18. Kumar, B. P. & Branner, G. R. Design of unequally spaced arrays for performance improvement. *IEEE Trans. Antennas Propag.* **47**, 511–523 (1999).

19. Yang, T. Y., Hong, W. & Zhang, Y. Wideband millimeter-wave substrate integrated waveguide cavity-backed rectangular patch antenna. *IEEE Antennas Wirel. Propag. Lett.* **13**, 205–208 (2014).

20. Li, J. X. *et al.* Cavity backed dual slot antenna for gain improvement. *Microw. Opt. Technol. Lett.* **52**, 2767–2769 (2010).

21. Mitha, T. & Pour, M. Principles of adaptive element spacing in linear array antennas. *Sci. Rep.* **11**, 1–11 (2021).

22. He, Y., Li, Y., Sun, W., Zhang, Z. & Chen, P.-Y. Dual linearly polarized microstrip antenna using a slot-loaded TM 50 mode. *IEEE Antennas Wirel. Propag. Lett.* **17**, 2344–2348 (2018).

23. Jin, L. *et al.* A novel dual-polarized gain-enhanced microstrip patch antenna. *Electromagnetics* **43**, 137–150 (2023).

24. Squadrito, P., Zhang, S. & Pedersen, G. F. Wideband or dual-band low-profile circular patch antenna with high-gain and sidelobe suppression. *IEEE Trans. Antennas Propag.* **66**, 3166–3171 (2018).

25. Aghabeyki, P., Moradi, G. & SarrafShirazi, R. Low-profile ring slot SIW antenna based on higher-order cylindrical cavity modes. *IET Microw. Antennas Propag.* **14**, 1779–1785 (2020).

Acknowledgements

Author contributions

Conceptualization, Meha Agrawal (M.A.), Yadav Ravi (Y.R.); Data curation, M.A., Y.R.; Formal analysis. M.A., Y.R.; Funding acquisition S.K (Slawomir Koziel) and Anna Pietrenko-Dabrowska (A.P.D.); Visualization, M.A., Y.R.; Writing—original draft, M.A.; Writing—review and editing, Y.R., S.K, A.P.D.; Sofware and Resources, M.A., Y.R., S.K.; Supervision, M.A., S.K.

Competing interests

The authors declare no competing interests.

Additional information

Correspondence and requests for materials should be addressed to M.A.

Reprints and permissions information is available at www.nature.com/reprints.

Publisher's note Springer Nature remains neutral with regard to jurisdictional claims in published maps and institutional affiliations.